Research Square

Preprints are preliminary reports that have not undergone peer review.
They should not be considered conclusive, used to inform clinical practice,
or referenced by the media as validated information.

Forcing Dataset Updates Impact Regional but Not Global Earth Radiation Budget Trends

Chongxing Fan

cxfan@princeton.edu

Princeton University https://orcid.org/0000-0002-3434-937X

David Paynter

Geophysical Fluid Dynamics Laboratory https://orcid.org/0000-0002-7092-241X

Ryan J. Kramer

Geophysical Fluid Dynamics Laboratory https://orcid.org/0000-0002-9377-0674

Vaishali Naik

Geophysical Fluid Dynamics Laboratory https://orcid.org/0000-0002-2254-1700

Research Article

Keywords: Earth radiation budget, climate model, climate forcing, aerosol radiative effect

Posted Date: May 19th, 2026

DOI: https://doi.org/10.21203/rs.3.rs-9707648/v1

License: This work is licensed under a Creative Commons Attribution 4.0 International License.
Read Full License

Additional Declarations: The authors declare no competing interests.

Abstract

The availability of up-to-date forcing datasets is critical for reconciling Earth system model simulations with contemporary observations. With the newly released CMIP7 forcing dataset, which extends the historical record through 2021, this study provides the first systematic evaluation of how using updated forcings over the “middle-of-the-road” SSP2-4.5 scenario forcings influences the simulated radiation budget. The updated forcing dataset used in the atmosphere model does not improve the agreement between the simulated global-mean top-of-the-atmosphere radiation trends and the satellite-observed trends. Regionally, we identify pronounced shifts in radiative energy partitioning between atmosphere and surface. Specifically, during 2001 ~ 2021, accelerated reductions in sulfate and black carbon aerosols over East Asia drive a significant decline in atmospheric solar absorption that matches observations, while a substantial increase in organic aerosols at higher latitudes induces a localized increase in atmospheric absorption that does not match observations. The substantial influence of localized forcing changes on simulated regional climate underscores the necessity for routine updates of forcing datasets.

Significance Statement

To faithfully simulate and attribute climate change, global models rely on accurate, up-to-date dataset of human and natural climate drivers, collectively termed as forcings dataset. The previous standard dataset used to drive these models only extended through 2014. We evaluated whether using a newly updated forcing dataset, now extended through 2021, improves model simulation of Earth’s radiation budget. Globally, the update did not meaningfully improve the match between model and satellite trends. However, at the regional level, the updated data captured the effects of reduced air pollution over East Asia more accurately, while overestimating the effect of increased particles over Siberia. These findings highlight that routinely updating forcing datasets is essential for accurately representing regional climate changes.

1. Introduction

Climate models are essential tools for understanding Earth system dynamics and generating reliable predictions and projections of future climate evolution (1). Historical simulations and comparisons with observational records enable researchers to assess model fidelity and attribute observed climate variations to specific forcing agents (2, 3). These simulations require forcing datasets as fundamental inputs. The forcing datasets, which include time-dependent external inputs like well-mixed greenhouse gases, ozone, aerosols, solar irradiance, and volcanic emissions, serve to drive climate model simulations. As scientific understanding of the spatial and temporal evolution of anthropogenic and natural processes advances, these datasets are extended and updated, in turn influencing model simulations of historical and future climate change. Here, we assess the impact of the updated forcing datasets developed in support of the Coupled Model Intercomparison Project Phase 7 (CMIP7) (4) on simulations of the Earth’s radiation budget over the 1979 ~ 2021 period.

Beginning with CMIP6, a common suite of forcing datasets have been developed in a coordinated manner by subject-matter experts external to modeling centers and delivered via input4MIPs on approximately 5–7-year cycles (4–6). These standardized datasets are used by the international climate modeling community to understand, attribute and project changes in the Earth System. A specific challenge is that updates to the full dataset suite do not occur annually, and therefore models rely on constructed forcing conditions from future, hypothetical emission scenarios to extend the historical datasets in the interim (7). This implies that the historical simulations do not necessarily reflect actual observed trajectories of these climate drivers. Beyond expanded temporal coverage, updated forcing datasets often incorporate bias corrections, higher spatial resolution, and improved feature representation. These updates can exert a profound influence on simulated climate states, as demonstrated in the analyses of the transition from CMIP5 to CMIP6 (8, 9).

In preparation for the ongoing CERESMIP (10) and CMIP7 (11) experiments, the input4MIPs team has recently published the updated forcing datasets through and beyond 2021 (4), which allows the simulations in both protocols to extend until the planned end year of 2021. It is crucial to investigate the difference between the CMIP7 forcing dataset and the CMIP6 + scenario forcing combination (referred to as CMIP6 for simplicity thereafter), as well as the impact of the forcing update on climate simulations. Aside from forcing uncertainty into the long future, another interesting question is whether it is sufficient to use a scenario-based forcing necessary for the models to simulate the real-world conditions, or whether it is necessary to provide up-to-date forcing regularly for climate models to run up to the near present.

This study aims to deliver an initial assessment of the impact of the CMIP7 forcing dataset, specifically greenhouse gas forcing, aerosol forcing, and natural forcing including volcanic aerosols and solar irradiance, on the Earth’s radiation budget based on GFDL AM4 atmosphere-only climate simulations. The Earth's radiation budget is the fundamental driver of climate system dynamics. At the top of the atmosphere (TOA), the net balance of absorbed solar radiation (ASR) and outgoing longwave radiation (OLR), as well as its regional distribution, determines the global and local energy storage of the climate system. The surface radiation budget, as part of the surface energy budget, regulates surface temperature and governs heat transfer between atmosphere, land, and ocean, fundamentally driving local and regional weather phenomena. Therefore, analyzing the impact of forcing updates on Earth’s radiation budget serves as a primary indicator of the broader impacts on simulated climate states.

In addition, satellite observations provide a continuous record of the TOA energy budget through the present (12, 13), facilitating a direct comparison between model-simulated radiative fluxes and the observational records. In general, CMIP6 models underestimate the net TOA radiation trend over the last two decades when compared to the CERES (Clouds and the Earth’s Radiant Energy System) (14, 15) observations, regardless of whether they utilize fully coupled configurations or Atmospheric Model Intercomparison Project (AMIP) (16) simulations with prescribed sea surface temperatures and sea ice concentrations (17–21). This underestimation has been attributed to an insufficient TOA shortwave (SW) absorption trend within the models. Beyond model physics uncertainty, there is little understanding of

the extent to which forcing dataset uncertainty may affect these observed biases in the simulated radiation budget. On the other hand, limited research focused on model-simulated surface radiative fluxes and atmospheric radiative absorption and compared them to observational records.

In this study, we assess the impact of CMIP7 forcing updates on Earth's radiation budget by first comparing the GFDL AM4 (22, 23) runs with CMIP7 forcing against control simulations that use the CMIP6 historical forcings extended to 2021 by the "middle-of-the-road" SSP2-4.5 future scenario forcings (Figures S1-S5) (24), which assumes the world does not shift markedly from historical patterns over the coming decades. Simulated TOA and surface radiative fluxes were compared to the CERES satellite observations. Despite the temporal coverage of the forcing dataset spanning from 1850 to near present, here our analyses focus on the CERES period of 2001 ~ 2021 and the full AMIP simulation period of 1979 ~ 2021. Here, we report that the CMIP7 forcing dataset minimally alters simulated global net TOA radiation trends and variability, which remain significantly below satellite observations. (Section 3). However, it introduces a decrease in atmospheric SW absorption and a consequent increase in downwelling surface SW radiation, which is attributable to aerosols (Section 3). Regionally, a marked reduction in sulfate and black carbon over East Asia reduces atmospheric absorption and brings the model into closer alignment with observations (Section 4). While an abrupt increase in organic aerosols over higher latitudes—such as Siberia—occurs around 2020 and causes a corresponding increase in atmospheric SW absorption, satellite data does not fully support the magnitude of this shift (Section 4).

2. Impact of Forcing Update on Global Radiation Budget

Comparing the CMIP7 forcing dataset to CMIP6, the time series of GHG concentrations (including CO_2, CH_4, N_2O, and various CFCs) closely align during the overlapping period (1979 ~ 2014). Post-2014, compared to the SSP2-4.5 projections, the updated forcing dataset reports slightly less CO_2 and CH_4, along with slightly more N_2O and CFCs, by up to 3% in concentration relatively and consequently ~ 0.01 W/m^2 in instantaneous radiative forcing (IRF; Figure S1). The input total solar irradiance in the CMIP7 forcing dataset increases by an average of 0.57 W/m^2 relative to the CMIP6 dataset over the period of 1979 ~ 2021. The corresponding linear trend is adjusted from − 0.16 W/m^2/decade in the CMIP6 dataset to − 0.11 W/m^2/decade in the CMIP7 dataset (Figure S2). The updated stratospheric volcanic forcing dataset reports enhanced forcing for the historical eruptions including the 1991 eruption of Mount Pinatubo. The input SW AOD and LW AOD increase by up to 16% and 25% for this event, respectively. The updated forcing dataset also records small post-2014 eruptions (Figure S3). Significant revisions are found in the new anthropogenic aerosol emissions dataset. The most notable features in the updated dataset include reversed black carbon emission trend from positive to negative over East Asia, increasing black carbon emission over higher latitudes, widespread increase of organic matter emission over high-latitude Northern Hemisphere due to biomass burning, and enhanced sulfate reduction since 2008 (driven by controls in East Asia) with a notable sharp dip around 2020 attributable to reduced ship emissions (Figures S4-S5).

Inspecting the period of 2001–2021 when CERES observations are available, after updating the forcing dataset to CMIP7, the ensemble of GFDL AM4 simulations reports a small decrease relative to the CMIP6 simulation in mean net TOA radiation imbalance (1.03 W/m^2 to 0.86 W/m^2; Fig. 1a), bringing it closer to the mean net TOA radiation imbalance in the CERES observations (0.76 W/m^2). However, the ensemble mean TOA radiative flux trends are insignificantly modified by updating the forcing from CMIP6 + SSP2-4.5 to CMIP7 (Fig. 1a-c). The linear trend of net TOA radiation from 2001 to 2021 in the CMIP7 simulations is adjusted down from 0.18 ± 0.10 W/m^2/decade in the CMIP6 simulations to 0.12 ± 0.11 W/m^2/decade (Table 1). Regardless of the choice of the forcing datasets, the trend in modeled net TOA radiation remains significantly lower than the CERES-observed trends (0.44 ± 0.13 W/m^2/decade; Fig. 1a; Table 1). As echoed in previous studies (17, 19), such an underestimation in net TOA radiation trend, which is widespread among many AMIP models, is primarily dominated by the underestimation of the TOA absorbed solar radiation trend (Fig. 1c). CERES reports a strong increase in solar absorption by 0.67 ± 0.11 W/m^2/decade from 2001 to 2021, while the latest CMIP7 AM4 simulations produce only half of the CERES trend (0.35 ± 0.08 W/m^2/decade; Table 1). It is important to note that even though the long-term trends do not compare well, the model captures the SW TOA variance in most of the period except the beginning (pre ~ 2003) and the end (post ~ 2017) periods (Fig. 1c). Both sets of simulations capture the LW TOA variance as well (Fig. 1b). The all-sky LW TOA absorption trend in the CMIP7 simulations becomes more negative than that in CMIP6 simulations and closer to the CERES-observed trend.

Table 1
Linear trends of TOA fluxes, surface fluxes, and atmospheric absorption in CERES observations and the ensemble mean of model simulations over the period of 2001–2021 in the unit of W/m^2/decade. The uncertainty values are 95% confidence intervals.

	CERES EBAF Ed4.2.1	GFDL AM4 CMIP7	GFDL AM4 CMIP6
TOA			
All–sky Net	0.44 ± 0.13	0.12 ± 0.11	0.18 ± 0.10
All–sky LW	−0.24 ± 0.10	−0.23 ± 0.07	−0.19 ± 0.08
All–sky SW	0.67 ± 0.11	0.35 ± 0.08	0.37 ± 0.08
Clear–sky Net	0.44 ± 0.10	0.12 ± 0.07	0.17 ± 0.06
Clear–sky LW	0.12 ± 0.07	−0.09 ± 0.06	−0.09 ± 0.06
Clear–sky SW	0.32 ± 0.07	0.22 ± 0.05	0.26 ± 0.05
Surface			
All–sky Net	0.02 ± 0.12	0.40 ± 0.08	0.36 ± 0.08
All–sky LW	−0.37 ± 0.10	0.30 ± 0.06	0.33 ± 0.06
All–sky SW	0.39 ± 0.13	0.10 ± 0.10	0.02 ± 0.09
Clear–sky Net	0.01 ± 0.12	0.42 ± 0.08	0.38 ± 0.07
Clear–sky LW	0.00 ± 0.08	0.48 ± 0.06	0.51 ± 0.05
Clear–sky SW	0.01 ± 0.10	−0.06 ± 0.07	−0.12 ± 0.06
Atmospheric Absorption			
All–sky Net	0.42 ± 0.12	−0.28 ± 0.09	−0.17 ± 0.09
All–sky LW	0.13 ± 0.13	−0.53 ± 0.12	−0.52 ± 0.11
All–sky SW	0.29 ± 0.06	0.25 ± 0.04	0.35 ± 0.04
Clear–sky Net	0.43 ± 0.11	−0.30 ± 0.08	−0.21 ± 0.08
Clear–sky LW	0.12 ± 0.12	−0.57 ± 0.10	−0.60 ± 0.10
Clear–sky SW	0.32 ± 0.06	0.27 ± 0.04	0.38 ± 0.04

The ensemble mean surface net radiative flux anomalies align closely between CMIP7 and CMIP6 simulations after the year 2000. Simulated surface LW fluxes in both cases track each other with the difference of linear trend less than 0.03 W/m^2/decade (Fig. 1e; Table 1). The surface net SW radiation trend from 2001 to 2021 is adjusted up from 0.02 ± 0.09 W/m^2/decade in the CMIP6 simulations to 0.10

± 0.09 W/m^2/decade in the CMIP7 simulations (Fig. 1f), which is attributable to surface downward SW radiation trend increase from − 0.19 ± 0.10 W/m^2/decade to − 0.08 ± 0.10 W/m^2/decade. CMIP7 simulations show relatively higher anomalies of positive surface net SW flux around 2010 when compared to CMIP6 simulations. Both sets of simulations yield comparable values for surface net SW flux in more recent years. As a result, for the 2011–2021 period, CMIP7 simulations exhibit a notably weaker surface SW trend (0.08 ± 0.25 W/m^2/decade) than CMIP6 simulations (0.38 ± 0.22 W/m^2/decade).

Interestingly, CERES-derived surface radiative fluxes show a stark contrast to model simulations, with substantially different trends (Table 1). CERES reports and a strong increase in incoming surface SW radiation (0.39 ± 0.13 W/m^2/decade from 2001 to 2021; Fig. 1f) and a compensating strong increase in outgoing surface LW fluxes (0.37 ± 0.10 W/m^2/decade from 2001 to 2021; Fig. 1e), resulting in a near balance of net surface radiative flux. Our model simulations, however, predict increasing LW and SW radiation into the surface. It should be noted that CERES surface fluxes are not direct measurements; rather, they are derived from a combination of observations and radiative transfer calculations that relies on inputs from reanalysis (15, 25, 26). Consequently, these surface products may carry significantly higher uncertainty than their TOA counterparts.

For the full AMIP period of 1979 ~ 2021 (Figure S6), differences in simulated TOA fluxes between the CMIP6 and CMIP7 simulations are small with the notable exception of the 1991 Pinatubo volcanic eruption. For this particular event, CMIP7 simulations report an increased amount of reflected solar radiation of approximately 0.6 W/m^2 (Figure S6c), which is partially offset by a 0.3 W/m^2 reduction in OLR (Figure S6b). This is consistent with stronger stratospheric volcanic AOD in the updated forcing dataset (Figure S3). Linear trend differences remain statistically insignificant within the 95% confidence interval. Regarding surface radiation budget, in addition to the volcanic eruptions, simulated surface net radiation is consistently lower in the CMIP7 simulations before 1997 by ~ 0.2 W/m^2, attributable to surface SW radiation differences. For the full period of 1979 ~ 2021, GFDL AM4 CMIP7 simulations report a significantly stronger surface net radiation trend (0.38 ± 0.04 W/m^2/decade) than the CMIP6 counterparts (0.29 ± 0.04 W/m^2/decade) due to a more positive SW radiation trend (0.03 ± 0.05 W/m^2/decade in CMIP7 compared to − 0.06 ± 0.04 W/m^2/decade in CMIP6; Figure S6f). Atmospheric radiative absorption, calculated by differentiating the incoming TOA radiative flux and the net surface radiative flux, shows a weaker increase in the CMIP7 simulations as a result (Figure S6i).

To fully account for uncertainty from internal variability, trend differences between CMIP6 and CMIP7 were calculated using all possible combinations (25 pairs) of five ensemble members from each generation. Figure 2 presents violin plots of the trend changes (CMIP7 minus CMIP6) in all-sky and clear-sky radiative fluxes at both the TOA and surface, alongside changes in atmospheric absorption. Also included are trend differences for the aerosol indirect radiative effect (IRE), which we derived by subtracting the clean-sky flux (excluding aerosols) from the all-sky flux. As previously discussed, shifting from the use of CMIP6 to CMIP7 forcing in GFDL AM4 results in minimal changes to TOA flux trends.

However, CMIP7 simulations exhibit a more negative trend in atmospheric SW absorption (change of − 0.07 W/m^2/decade for all-sky flux), alongside a pronounced increase in downward surface SW radiation (change of + 0.11 W/m^2/decade for all-sky flux) (bottom left panel of Fig. 2). Out of 25 pairs of simulations, 24 pairs indicate significantly less atmospheric SW absorption (at 95% confidence level) in the CMIP7 simulation than the corresponding CMIP6 simulation. Differences in downward surface SW fluxes are more statistically significant under clear-sky conditions, where the absence of cloud noise clarifies the signal. The reduction of atmospheric SW absorption and the resulting increase in downward surface SW radiation in CMIP7 simulations originate from the aerosol IRE contributions. Specifically, within CMIP7 simulations, the aerosol IRE contributes a trend increment of + 0.05 W/m^2/decade to surface SW radiation and − 0.07 W/m^2/decade to atmospheric SW absorption (bottom right panel of Fig. 2). At the TOA, the aerosol IRE also reflects significantly more SW radiation (0.02 W/m^2/decade) in CMIP7. Differences in all-sky and clear-sky shortwave (SW) top-of-atmosphere (TOA) fluxes remain generally negative; however, they lack statistical significance, likely due to noise introduced by the internal variability of water vapor and clouds across ensemble members.

3. Regional Radiative Flux Differences Attributable to the Updated Anthropogenic Aerosol Forcing

We now examine the relationship of the reduction of atmospheric SW absorption and the anthropogenic aerosol forcing updates from CMIP6 to CMIP7. The radiation module in GFDL AM4 calculates aerosol optical depth (AOD) and other optical properties based on input aerosol loadings of different species. These properties define the absorption and scattering characteristics of the atmosphere. Between 1979 and 2014, compared to the CMIP6 simulations, CMIP7 simulations report lower mean AOD by 0.002 in GFDL AM4 (Fig. 3a). Such lower AOD in CMIP7 relative to CMIP6 simulations is more prominent after the year 2008 (lower by 0.006). After 2014, forced by the SSP2-4.5 scenario projection, AOD in the CMIP6 simulations declines steadily with minimal interannual variability. In contrast, CMIP7 AOD exhibits significant fluctuations, including a sharp decrease in 2020 followed by a quick rebound after 2020 (Fig. 3a). This results from a combination of biomass burning in recent years and a remarkable decrease in sulfate emission from ships (Figure S4). Regionally, inspecting the recent 21 years (2001 ~ 2021), CMIP7 reports a much stronger decrease of AOD in East Asia (Fig. 3b) driven primarily by the reduced sulfate emission and secondarily by the reduced black carbon and organic aerosols (Fig. 3c). These forcing updates reflect substantial aerosol reductions resulting from emission policies adopted in East Asia (27). As a result, AOD trend in CMIP7 simulations aligns more closely with MODIS-observed trends (Figure S7). On the other hand, compared to the CMIP6 forcing dataset, the CMIP7 dataset adjusts up the AOD trend over the Siberia region (Fig. 3b) with major contributions from increasing concentration of organic aerosols (Fig. 3c). This could be related to the wildfire emission in this region (Figure S5) (28).

The impact of anthropogenic aerosol forcing updates on all-sky TOA radiation is minimal even at the regional scale (Fig. 3d). However, the bipolar pattern of the AOD differences, characterized by reduced aerosols in East Asia and more aerosols over Siberia, translates into a corresponding pattern in

atmospheric SW absorption, where East Asia sees less absorption and the East Siberia region sees more absorption (Fig. 3e). Because of the latitudinal distribution of the incoming SW radiation, the magnitude of the trend difference is larger over East Asia than over Siberia. When averaged globally, the decrease in atmospheric SW absorption is more dominant, explaining the decreasing trend in CMIP7 simulations (Fig. 2). To isolate the impact of individual forcing agents, we conducted single-forcing experiments in which greenhouse gases, aerosols, or natural factors (volcanic and solar) were varied while all other forcings remained fixed at 1850 levels. Only when historical variation of aerosol forcing is included in the simulations do the decrease of atmospheric SW absorption and the associated increase of downward surface SW radiation show up, suggesting that the trend differences in anthropogenic aerosol loading explain nearly all the trend differences in radiative fluxes between the two generations (Figures S8 and S9). While CMIP6 simulations show a global increase in atmospheric SW absorption, CMIP7 accurately captures the SW absorption decrease observed by CERES over East Asia during the last two decades (Figure S7). However, the atmospheric SW absorption produced by CMIP7 over East Siberia is considerably higher than that indicated by CERES observations (Figure S7).

Now we focus on the three hot spots identified in Fig. 3: East Asia (15ºN ~ 55ºN, 100ºE~145ºE) where widespread AOD decrease and the corresponding atmospheric SW absorption decrease are observed in the CMIP7 simulations, East Siberia (55ºN ~ 70ºN, 100ºE~145ºE) where large-scale AOD increase and atmospheric SW absorption increase are found, and a portion of North America (30ºN ~ 60ºN, 110ºW ~ 70ºW) that has witnessed AOD decrease over East Coast but also increasing wildfires in recent years. From the time series, both total AOD and absorbing AOD (Figure S10) over East Asia is lower by ~ 0.04 after approximately 2008 in the CMIP7 simulations, and such relatively low AOD continues after 2014. Aerosol reductions have distinct effects on radiative transfer: the decrease in absorbing aerosols directly lowers shortwave (SW) radiation absorption in the atmosphere, while the decrease in scattering aerosols reduces the amount of SW radiation reaching the surface and lengthening the path photons travel in the atmosphere (29). Overall, atmospheric SW absorption is observed to have decreased in the last 10 years. Because flux anomalies are calculated over the 2001 ~ 2021 period, decreasing SW absorption after 2008 is translated into larger flux absorption anomalies before 2008 in the time series. The linear trend of atmospheric SW absorption reverses from 0.86 ± 0.17 W/m^2/decade to -0.38 ± 0.14 W/m^2/decade. In this particular case, CMIP7 simulations report better agreement with MODIS-observed AOD and CERES-derived SW absorption (Fig. 4).

Over East Siberia, the more positive AOD trend in the CMIP7 simulations as seen from Fig. 3 is caused by AOD increase after 2015. The SSP2-4.5 scenario forcing is unable to capture the large interannual variability of aerosol forcing. Meanwhile, CMIP7 forcing dataset reports a sharp increase in biomass burning emissions around 2020 (Figs. 3, S4, S5, and S11). The model forced by such an increase in aerosol loading produces an expected sharp increase in atmospheric SW absorption and a remarkable decrease in absorbed SW radiation at the TOA. Comparing model simulations of the TOA absorbed solar radiation (ASR) directly to the CERES data is challenging because of the significant variability in the CERES observations caused by limited spatial sampling. Qualitatively speaking, an interesting finding is that TOA ASR in the CERES observations shows a gradual and gentle increase over East Siberia, with no

notable deviations reported. The sharp increase of atmospheric SW absorption at the end of the time series is also absent from the CERES-derived values.

Over North America, CERES observations report a very large variability in TOA ASR with little linear trend, while the model simulations produce slightly increasing absorbed solar radiation in the last two decades with smaller interannual variation. Correspondingly, MODIS AOD has a flatter trend than the model-simulated AOD. Poor data sampling may contribute to such discrepancies (Figure S7). Atmospheric SW absorption, however, agrees better between the model simulations and the observations. Notably at the end of the time series, an abrupt increase in AOD was recorded by MODIS and a corresponding increase in atmospheric SW absorption was reported by CERES. In this specific event, CMIP7 simulations reproduce the AOD increase in relative scale and accurately match atmospheric SW absorption anomalies in CERES observations.

4. Discussion

This study conducts a comprehensive TOA and surface radiation budget analysis and compares the results when using the up-to-date CMIP7 forcing datasets to the ones when using the CMIP6 forcing datasets extended by the middle-of-the-road scenario forcing dataset (i.e., SSP2-4.5) in GFDL AM4. Updating to CMIP7 forcing improves the model's mean net TOA radiation imbalance, bringing it closer to CERES observations. However, it does not affect the simulated TOA radiation trend, and GFDL AM4 still significantly underestimates the observed trend in net TOA radiation with the bias stemming from the SW component. Within the Earth system, the model with CMIP7 forcing tends to produce less SW absorption in the atmosphere and more SW radiation into the surface by 0.05 W/m^2 per decade on global average, especially in the last 15 years. Regionally, the differences of linear trends feature a strong dipole: a significant decrease of atmospheric SW absorption by up to 4 W/m^2 per decade over East Asia and a moderate increase by 1 W/m^2 per decade over East Siberia. These differences are attributable to the aerosol forcing updates. In the CMIP7 forcing dataset, reduced sulfate and black carbon emissions over East Asia allow more SW radiation reaching the surface and diminish the strength of atmospheric absorption, respectively. This effect outweighs the impact of increasing organic aerosol emission over Siberia, where the lower incident solar radiation at high latitudes limits their radiative impact.

Our findings suggest that TOA radiation budget in the AMIP simulations is minimally modified by the updates of the CMIP7 forcing dataset at both global and regional scales. At least in terms of the Earth's radiation trends, the CMIP7 simulations align closely with the "middle-of-the-road" scenario in CMIP6 projections very well. Minor deviations in atmospheric concentrations in the real world—specifically a small decrease in CO_2, N_2O, and CH_4, alongside a small increase in CFCs (Figure S1)—do not alter the simulated Earth's radiation budget as represented by this specific scenario. The same applies to other forcing agents from the global perspective (Figures S2–S5). Comparing AMIP simulations to the CERES observations, underestimation of absorbed solar radiation at the TOA is expected to persist after updating the CMIP7 forcing dataset. The degree to which AMIP models in the upcoming CMIP7 experiment could yield results closer to the CERES-observed values is now contingent upon the

advancements made in model physics since the previous generation of models. Meanwhile, although CMIP7 sticks to the use of PCMDI SST and sea ice dataset as in the CMIP6 experiment, new evidence shows that alternative SST and sea ice products exist that could produce stronger clear-sky TOA absorbed solar radiation in the AMIP simulations (Figure S12) (20). In addition to routinely extending the time series, future updates to input forcing datasets should also include evaluation of alternative forcing products and assess their uncertainty and impact to the model simulations.

From the regional perspective, the updated forcing dataset incorporates the latest high-resolution real-world emission data, leading to substantial modifications in the regional flux trend. This is particularly evident for short-lived species characterized by high spatial and temporal heterogeneity. General underestimation of sulfate and black carbon reduction over East Asia and the missing sharp increase of organic aerosol over East Siberia and North America are prominent examples in the scenario forcing driven simulations. Consistent with physical intuition, these changes lead to corresponding radiation response in the AMIP models. The simulated atmospheric SW absorption agrees well with CERES-derived values in East Asia (Fig. 4). The consequent less atmospheric SW absorption of ~ 4 W/m^2 per decade over East Asia is coincident with a slight increase in simulated precipitation and evaporation after 2008 (Figure S13). The reverse is true for the higher-latitude Siberia region, especially over the last 5 years. However, the sharp reduction of TOA and surface SW radiation over East Siberia around 2020 do not match the CERES records (Fig. 4). If the updated forcing data is accurate and reflects real-world conditions, these inconsistencies suggest that either the current atmosphere models are missing physical processes that could mask the signal, or the CERES observations are failing to capture the signal. Future investigation on this particular issue is warranted. Regardless of the underlying reasons, beyond the global Earth's energy imbalance, it is crucial to compare model-simulated radiation with observations at the regional scale and at the process level. This is powerful for identifying potential model issues, as regional signals can often be significantly stronger than their globally averaged counterparts.

This study investigates the radiative response of one particular AMIP model to the updated CMIP7 forcing. The same experiments should be conducted across a range of other AMIP models to fully evaluate and understand how forcing updates affect AMIP simulations. One step further, unlike AMIP simulations where sea surface temperature and sea ice are prescribed by historical observations, these surface state variables will also respond to the forcing updates in the coupled model simulations, both in mean value and its spatial pattern. Feedback processes may be triggered to further adjust the radiation budget and induce associated climate response. Evaluations of the forcing updates in fully coupled Earth system models covering the full period since the preindustrial level (1850 ~ 2021) are thus valuable to provide a complete and comprehensive assessment of the CMIP7 forcing dataset and inspire future improvements to both model inputs and model physics.

5. Materials and Methods

5.1. CMIP Forcing Dataset

CMIP forcing datasets provide a standardized set of inputs for participating models, ensuring that differences in results are attributed to internal model physics rather than different assumptions about external drivers. The recently released forcing dataset for use in CMIP7 DECK experiments consists of twelve components (4), five of which are used to force the AMIP runs in this study (Table 2).

Table 2
Details of CMIP6 and CMIP7 forcing datasets used in our simulations.

Anthropogenic short-lived climate forcer (SLCF)	**CMIP6**	**CMIP7**
	CEDS-2017-05-18 (44)	**CEDS-CMIP-2025-04-18 (45)**
Open biomass burning emissions	VUA-CMIP-BB4CMIP6-1-2 (46)	DRES-CMIP-BB4CMIP7-2-1 (47)
Greenhouse gas concentrations (GHGs)	UoM-CMIP-1-2-0 (48)	CR-CMIP-1-0-0 (49)
Stratospheric volcanic SO_2 emissions and aerosol optical properties	IACETH-SAGE3lambda-3-0-0 (50)	UOEXETER-CMIP-2-2-1 (51)
Solar irradiance	SOLARIS-HEPPA-CMIP-3-2 (52)	SOLARIS-HEPPA-CMIP-4-6 (53)
Sea surface temperature (SST) and sea ice (SI) boundary forcing	HadISST 2.4.0.0 SST and HadISST 2.2.4.0 SI (30)	
Ozone forcing	UReading-CCMI-1-0 (54)	

All other forcing remains the same between CMIP6 and CMIP7 simulations. CMIP7 continues to use the PCMDI-AMIP sea surface temperature and sea ice dataset as CMIP6; while the version has been updated and the records extended, these modifications are expected to yield negligible differences in model simulations. However, in this study, we used HadISST 2.4.0.0 SST and HadISST 2.2.4.0 SI (30) in all simulations instead of the recommended PCMDI-AMIP 1.1.10 dataset (31). In the particular case of GFDL AM4, the simulated clear-sky TOA SW trend is more consistent with the CERES observations when the HadISST 2.x forcing dataset is used (Figure S12) (20). Because the CMIP7 ozone concentrations had not yet been stably finalized at the time of simulation, we kept using the CMIP6 + SSP2-4.5 ozone forcing dataset in all simulations. GFDL AM4 uses static vegetation, so land use forcing dataset is not utilized here.

5.2. CERES EBAF Ed4.2.1

The Clouds and Earth's Radiant Energy System (CERES) Energy Balanced and Flux (EBAF) product offers observation-based monthly gridded radiative fluxes (14, 15). The source of data includes two CERES instruments onboard Terra since March 2000, with the addition of another two instruments onboard Aqua satellite after July 2002, and is switched to the sole CERES instrument onboard NOAA-20 satellite after April 2022. TOA radiative fluxes at the global scale are extrapolated and averaged with the aid of geostationary satellites (14). An objective adjustment of global-mean net fluxes is applied to the EBAF

product to remain consistent with independent estimates of Earth's energy imbalance derived from ocean heat content inventories (14). The calculation of surface radiative fluxes requires a combination of the direct TOA measurements and radiative transfer modeling with reanalysis inputs from the Goddard Earth Observing System (GEOS) (15).

We compared our model output TOA fluxes against CERES EBAF Edition 4.2.1 (CERES EBAF-4.2.1) from 2001 to 2021, consisting of 21 full years. The product provides two versions of clear-sky fluxes, one that averages only over clear-sky scenes, and the other that applies the cloud clearing algorithm to compute clear-sky fluxes for all regions. We opted for the latter as it aligns better with the definition of clear-sky fluxes in climate models. Regardless of the choice, the clear-sky TOA flux trends from 2001 to 2021 are similar (Figure S12).

5.3. MODIS AOD

We used the Moderate Resolution Imaging Spectroradiometer (MODIS) Collection 6.1 Dark Target and Deep Blue products as the observational reference for AOD (32–34). Originally developed as a byproduct of atmospheric correction to improve land surface and ocean color measurements, the Dark Target algorithm has since been refined into a primary tool for quantifying global aerosol properties (35, 36). The retrieval is built on the physical principle that aerosols appear to brighten naturally dark scenes. Consequently, two distinct algorithms are developed: one optimized for the dark surfaces of the global ocean across visible and longer wavelengths, and another specifically for vegetated or dark-soiled land surfaces. AOD at 550 nm is then computed from radiative transfer model based on the aerosol retrievals. The Deep Blue product is designed to fill data gaps left by the Dark Target algorithm over bright land surfaces. By utilizing violet wavelengths, where most land surfaces exhibit low reflectance, the algorithm ensures these regions appear dark in this specific spectral range to the sensor for aerosol retrieval. Validation against the AERONET ground-based measurement demonstrates that the MODIS aerosol product shows a generally good performance with strong correlation and low error (32, 33, 37, 38).

Here, we used the monthly one-degree MODIS Level 3 product from Terra and Aqua satellites (i.e., MOD08_M3 and MYD08_M3). The combined Dark Target and Deep Blue AOD at 0.55 micron for land and ocean (AOD_550_Dark_Target_Deep_Blue_Combined_Mean_Mean) from the two products are averaged and analyzed.

5.4. GFDL AM4/LM4

In this study, we ran AMIP-compatible simulations using the GFDL AM4/LM4 model (22, 23), a state-of-the-art atmosphere/land model with a ~ 100 km horizontal grid and 33 vertical levels. When compared to the CERES observations, GFDL AM4 simulates slightly more reflected SW radiation and less emitted LW radiation at the TOA (~ 1 W/m^2) (22). Evaluation against a suite of surface-based and satellite observations demonstrates that GFDL AM4 shows good agreement with observed total AOD (39). Historical simulations were performed using two different sets of forcings: one based on CMIP7 and the other combining CMIP6 with SSP2-4.5, as described in Section 2.1. Both simulations span the period

from 1979 to 2021 and consist of five ensemble members each. For simplicity, these two simulation sets will be referred to as the CMIP7 and CMIP6 simulations hereafter.

To attribute the flux changes to different forcing agents, we designed and executed a series of single-forcing experiments in accordance with the CERESMIP protocol (10). The simulations include all forcing runs (amip), historical SST and sea ice only runs (amip-sst), aerosol forcing only runs (amip-aer), greenhouse gas only runs (amip-ghg), and natural forcing only runs (amip-nat). Details and results from the single-forcing experiments are discussed in the supplementary materials (Figures S8-S9).

5.5. Statistical Analysis

The analysis focuses on the monthly mean time series of TOA and surface broadband radiative fluxes. Global mean fluxes are computed by averaging the gridded fluxes weighted by grid point area. The model outputs are first regridded from their native resolution to a 1°×1.25° latitude-longitude grid and then averaged using cosine-of-latitude weighting. CERES fluxes are averaged using geodetic weighting, consistent with the procedure used by the CERES team, while assuming that the Earth is an oblate spheroid instead of a sphere. These weights are provided on the CERES website (https://ceres.larc.nasa.gov/data/general-product-info/#geodetic-zone-weights-information). For model simulations, the ensemble mean was calculated by averaging the five individual ensemble members. This is used in all figures except Figs. 2, S8, and S9.

To calculate flux anomalies for both model output fluxes and CERES-observed fluxes, the monthly climatology over the period from 2001 to 2021 is computed and subtracted from each time series. We used ordinary least squares (OLS) to estimate the linear trend, with uncertainties reported as 95% confidence intervals based on a *t*-distribution Wald test. This method was applied to both the global mean monthly anomalies and to individual grid points to generate a spatial trend map. We used the SciPy implementation of the linear regression (linregress) to conduct the analyses (40).

To account for the uncertainty associated with internal variability when comparing the CMIP7 and CMIP6 simulations, we calculated the differences for all 25 possible pairings, specifically between each ensemble member of the CMIP7 simulations and each member of the CMIP6 simulations. We applied the same linear trend analysis to each pair, reporting uncertainties as 95% confidence intervals. The violin plot illustrates the distribution of trend differences across the 25 pairs, representing uncertainty derived from internal variability. In the main text, we also evaluate the number of trend differences that reach statistical significance, which incorporates the uncertainty from the linear regression.

Declarations

Competing Interest:

The authors declare that they have no competing interests.

Classification

Physical Sciences – Earth, Atmospheric, and Planetary Sciences

Data and materials availability

All data are available in the main text or the supplementary materials. CMIP7 forcing datasets are summarized in the input4MIPs documentation website (https://input4mips-cvs.readthedocs.io/en/latest/) and can be downloaded following the individual links. CERES EBAF products can be downloaded at https://ceres.larc.nasa.gov/data/. MODIS data are distributed by the Level-1 and Atmosphere Archive and Distribution System Distributed Active Archive Center (https://ladsweb.modaps.eosdis.nasa.gov/) (41, 42). The source code of GFDL AM4 is available via Zenodo (43).

Author Contributions:

Conceptualization: CF, DP, RJK; Methodology: CF, DP, RJK; Investigation: CF, DP, RJK, VN; Visualization: CF; Supervision: DP; Writing—original draft: CF; Writing—review & editing: CF, DP, RJK, VN

Acknowledgments

We are grateful to Dr. John Dunne and Dr. Fabien Paulot for their constructive feedback and suggestions during the internal review process. We thank the CMIP Forcings Task Team for preparing and providing the CMIP7 forcing datasets. We also acknowledge the valuable efforts of Dr. Jing Feng, Dr. Eric Stofferahn, and Dr. Pu Lin in processing the CMIP7 forcing datasets specifically for GFDL models. This work was supported by GFDL computational resources. This report was prepared by Chongxing Fan under award NA23OAR4320198 from the National Oceanic and Atmospheric Administration, U.S. Department of Commerce. The statements, findings, conclusions, and recommendations are those of the author(s) and do not necessarily reflect the views of the National Oceanic and Atmospheric Administration, or the U.S. Department of Commerce. Chongxing Fan is also supported by the NOAA Climate Program Office, Earth's Radiation Budget (ERB) Program.

References

1. Intergovernmental Panel On Climate Change (IPCC) (2023) Climate Change 2021 – The Physical Science Basis: Working Group I Contribution to the Sixth Assessment Report of the Intergovernmental Panel on Climate Change, 1st edn. Cambridge University Press
2. Eyring V et al (2019) Taking climate model evaluation to the next level. Nat Clim Change 9:102–110

3. Gillett NP et al (2025) The Detection and Attribution Model Intercomparison Project (DAMIP v2.0) contribution to CMIP7. Geosci Model Dev 18:4399–4416
4. Durack PJ et al (2025) Earth System Forcing for CMIP7 and Beyond. Bull Am Meteorol Soc 106:E1580–E1588
5. Durack P et al (2018) Toward Standardized Data Sets for Climate Model Experimentation. *Eos* 99
6. Eyring V et al (2016) Overview of the Coupled Model Intercomparison Project Phase 6 (CMIP6) experimental design and organization. Geosci Model Dev 9:1937–1958
7. Naik V et al (2025) Climate models need more frequent releases of input data — here's how to do it. Nature 644:874–875
8. Fyfe JC, Kharin VV, Santer BD, Cole JNS, Gillett NP (2021) Significant impact of forcing uncertainty in a large ensemble of climate model simulations. *Proceedings of the National Academy of Sciences* 118, e2016549118
9. Holland MM et al (2024) New model ensemble reveals how forcing uncertainty and model structure alter climate simulated across CMIP generations of the Community Earth System Model. Geosci Model Dev 17:1585–1602
10. Schmidt GA et al (2023) CERESMIP: a climate modeling protocol to investigate recent trends in the Earth's Energy Imbalance. Front Clim 5:1202161
11. Dunne JP et al (2025) An evolving Coupled Model Intercomparison Project phase 7 (CMIP7) and Fast Track in support of future climate assessment. Geosci Model Dev 18:6671–6700
12. Loeb NG et al (2020) New Generation of Climate Models Track Recent Unprecedented Changes in Earth's Radiation Budget Observed by CERES. *Geophysical Research Letters* 47, e2019GL086705
13. Loeb NG et al (2024) Observational Assessment of Changes in Earth's Energy Imbalance Since 2000. *Surv Geophys* https://doi.org/10.1007/s10712-024-09838-8
14. Loeb NG et al (2018) Clouds and the Earth's Radiant Energy System (CERES) Energy Balanced and Filled (EBAF) Top-of-Atmosphere (TOA) Edition-4.0 Data Product. J Clim 31:895–918
15. Kato S et al (2018) Surface Irradiances of Edition 4.0 Clouds and the Earth's Radiant Energy System (CERES) Energy Balanced and Filled (EBAF) Data Product. J Clim 31:4501–4527
16. Gates WL et al (1999) An Overview of the Results of the Atmospheric Model Intercomparison Project (AMIP I). Bull Am Meteorol Soc 80:29–56
17. Raghuraman SP, Paynter D, Ramaswamy V (2021) Anthropogenic forcing and response yield observed positive trend in Earth's energy imbalance. Nat Commun 12:4577
18. Hodnebrog Ø et al (2024) Recent reductions in aerosol emissions have increased Earth's energy imbalance. Commun Earth Environ 5:1–9
19. Olonscheck D, Rugenstein M (2024) Coupled Climate Models Systematically Underestimate Radiation Response to Surface Warming. *Geophysical Research Letters* 51, e2023GL106909
20. Fan C, Paynter D, Kramer RJ, Lin P (2025) Sensitivity of Earth's Radiation Budget to Lower Boundary Condition Data Sets in Historical Climate Simulations. *Geophysical Research Letters* 52,

e2025GL115914

21. Myhre G, Hodnebrog Ø, Loeb N, Forster PM (2025) Observed trend in Earth energy imbalance may provide a constraint for low climate sensitivity models. Science 388:1210–1213
22. Zhao M et al (2018) The GFDL Global Atmosphere and Land Model AM4.0/LM4.0: 1. Simulation Characteristics With Prescribed SSTs. J Adv Model Earth Syst 10:691–734
23. Zhao M et al (2018) The GFDL Global Atmosphere and Land Model AM4.0/LM4.0: 2. Model Description, Sensitivity Studies, and Tuning Strategies. J Adv Model Earth Syst 10:735–769
24. O'Neill BC et al (2017) The roads ahead: Narratives for shared socioeconomic pathways describing world futures in the 21st century. Glob Environ Change 42:169–180
25. Smith GL et al (2011) Clouds and Earth Radiant Energy System (CERES), a review: Past, present and future. Adv Space Res 48:254–263
26. Kratz DP, Gupta SK, Wilber AC, Sothcott VE (2020) Validation of the CERES Edition-4A Surface-Only Flux Algorithms. J Appl Meteorol Climatology 59:281–295
27. Zhang Q et al (2019) Drivers of improved PM2.5 air quality in China from 2013 to 2017. *Proceedings of the National Academy of Sciences* 116, 24463–24469
28. Huang X et al (2024) Escalating Wildfires in Siberia Driven by Climate Feedbacks Under a Warming Arctic in the 21st Century. *AGU Advances* 5, e2023AV001151
29. Haywood JM, Ramaswamy V (1998) Global sensitivity studies of the direct radiative forcing due to anthropogenic sulfate and black carbon aerosols. J Geophys Res 103:6043–6058
30. Kennedy JJ, Rayner NA, Atkinson CP, Killick RE (2019) JGR Atmos 124:7719–7763An Ensemble Data Set of Sea Surface Temperature Change From 1850: The Met Office Hadley Centre HadSST.4.0.0.0 Data Set
31. Taylor KE, Williamson D, Zwiers F (2000) The sea surface temperature and sea-ice concentration boundary conditions for AMIP II simulations. Lawrence Livermore National Laboratory
32. Levy RC et al (2015) Towards a long-term global aerosol optical depth record: applying a consistent aerosol retrieval algorithm to MODIS and VIIRS-observed reflectance. Atmos Meas Tech 8:4083–4110
33. Levy RC et al (2013) The Collection 6 MODIS aerosol products over land and ocean. Atmos Meas Tech 6:2989–3034
34. Gupta P, Levy RC, Mattoo S, Remer LA, Munchak LA (2016) A surface reflectance scheme for retrieving aerosol optical depth over urbansurfaces in MODIS Dark Target retrieval algorithm. Atmos Meas Tech 9:3293–3308
35. Kaufman YJ et al (1997) Passive remote sensing of tropospheric aerosol and atmospheric correction for the aerosol effect. J Geophys Res 102:16815–16830
36. Tanré D, Kaufman YJ, Herman M, Mattoo S (1997) Remote sensing of aerosol properties over oceans using the MODIS/EOS spectral radiances. J Geophys Res 102:16971–16988

37. Huang Y et al (2019) Evaluation and Comparison of MODIS Collection 6.1 and Collection 6 Dark Target Aerosol Optical Depth over Mainland China Under Various Conditions Including Spatiotemporal Distribution, Haze Effects, and Underlying Surface. Earth Space Sci 6:2575–2592
38. Wei J, Li Z, Peng Y, Sun L (2019) Collection 6.1 aerosol optical depth products over land and ocean: validation and comparison. Atmos Environ 201:428–440
39. Gliß J et al (2021) AeroCom phase III multi-model evaluation of the aerosol life cycle and optical properties using ground- and space-based remote sensing as well as surface in situ observations. Atmos Chem Phys 21:87–128
40. Virtanen P et al (2020) SciPy 1.0: fundamental algorithms for scientific computing in Python. Nat Methods 17:261–272
41. MODIS Atmosphere Science Team, MYD08_M3 MODIS/Aqua Aerosol Cloud Water Vapor Ozone Monthly L3 Global 1Deg CMG (2017) NASA Level 1 and Atmosphere Archive and Distribution System Distributed Active Archive Center. https://doi.org/10.5067/MODIS/MYD08_M3.061
42. MODIS Atmosphere Science Team, MODIS/Terra Aerosol Cloud Water Vapor Ozone Monthly L3 Global 1Deg CMG (2017) NASA Level 1 and Atmosphere Archive and Distribution System Distributed Active Archive Center. https://doi.org/10.5067/MODIS/MOD08_M3.061
43. Zhao M, NOAA-GFDL/AM4 (2018) : AM4 Paper Release. https://doi.org/10.5281/ZENODO.1199643. Deposited 15 March 2018.
44. Hoesly RM et al (2014) Historical (1750– anthropogenic emissions of reactive gases and aerosols from the Community Emissions Data System (CEDS). *Geosci. Model Dev.* 11, 369–408 (2018)
45. Hoesly R et al CEDS v_2025_04_18 Gridded Emissions Data 0.5 degree. Zenodo. https://doi.org/10.5281/ZENODO.15127477. Deposited 18 April 2025.
46. van Marle MJE et al (2017) Historic global biomass burning emissions for CMIP6 (BB4CMIP) based on merging satellite observations with proxies and fire models (1750–2015). Geosci Model Dev 10:3329–3357
47. van Marle M, van der Werf G (2025) Deposited, input4MIPs.CMIP7.DRES.DRES-CMIP-BB4CMIP7-2-0. Oak Ridge National Laboratory (ORNL), Oak Ridge, TN (United States). https://doi.org/10.25981/ESGF.INPUT4MIPS.CMIP7/2524040
48. Meinshausen M et al (2017) Historical greenhouse gas concentrations for climate modelling (CMIP6). Geosci Model Dev 10:2057–2116
49. Nicholls Z, Meinshausen M, Pflüger M, Lewis J CMIP GHG Forcing. Zenodo. https://doi.org/10.5281/ZENODO.14892947. Deposited 28 February 2025.
50. Revell LE et al (2017) Impacts of Mt Pinatubo volcanic aerosol on the tropical stratosphere in chemistry–climate model simulations using CCMI and CMIP6 stratospheric aerosol data. Atmos Chem Phys 17:13139–13150
51. Aubry TJ et al (2025) Stratospheric aerosol forcing for CMIP7 (part 1): Optical properties for pre-industrial, historical, and scenario simulations (version 2.2.1). [Preprint] Available at:

https://egusphere.copernicus.org/preprints/2025/egusphere-2025-4990/ [Accessed 23 March 2026]

52. Matthes K et al (2017) Solar forcing for CMIP6 (v3.2). Geosci Model Dev 10:2247–2302
53. Funke B et al (2024) Towards the definition of a solar forcing dataset for CMIP7. Geosci Model Dev 17:1217–1227
54. Hegglin M, Kinnison D, Lamarque J-F, Plummer D CCMI ozone in support of CMIP6 - version 1.0. Earth System Grid Federation. https://doi.org/10.22033/ESGF/INPUT4MIPS.1115. Deposited 2016.

Figures

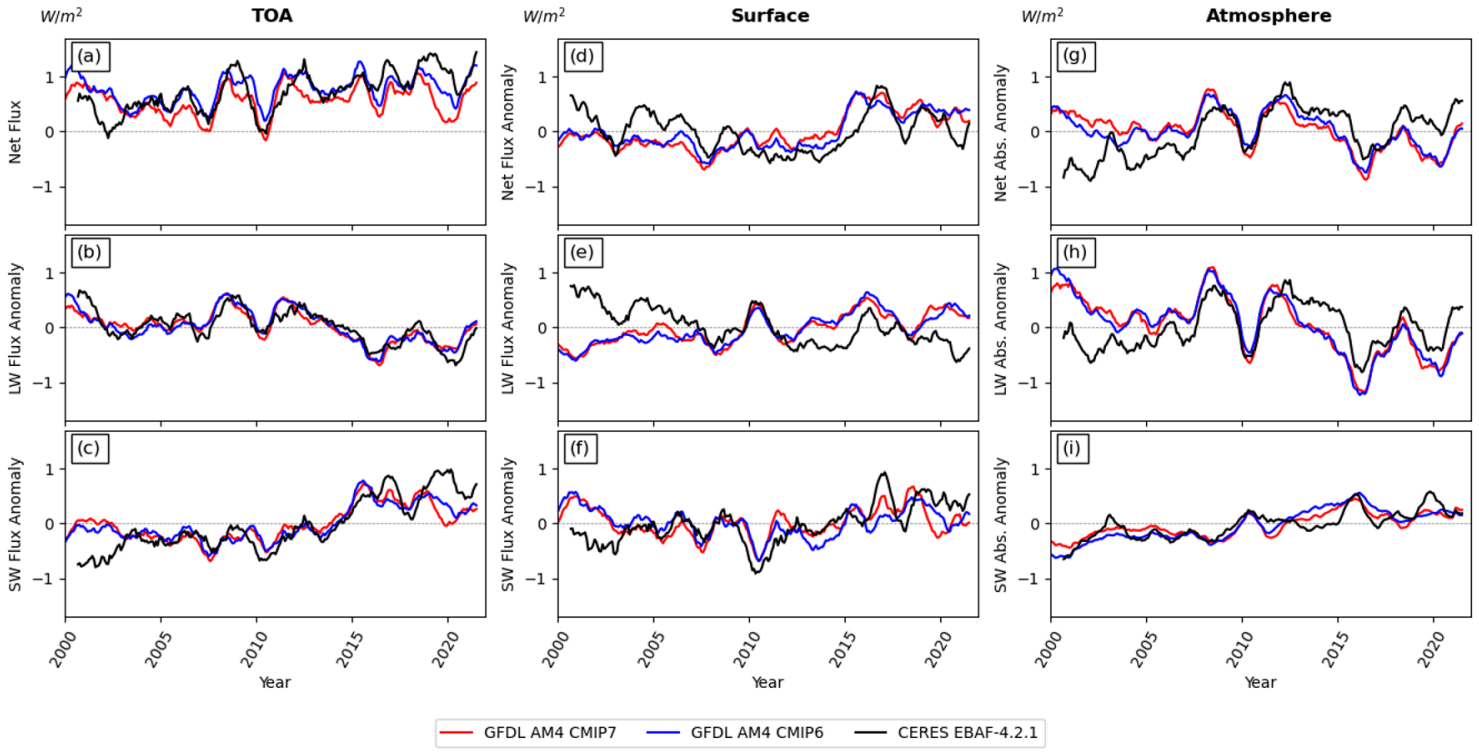


Figure 1

Monthly global mean anomalies of all sky TOA (left column) and surface (middle column) radiative fluxes from CERES EBAF-4.2.1 observations (black) and ensemble mean of GFDL AM4 historical simulations forced by CMIP6 forcings (blue) and CMIP7 forcings (red). Atmospheric radiative absorption (right column) is computed as the difference of incoming TOA flux and downward surface flux. Net fluxes (top row) are also decomposed into longwave components (middle row) and shortwave components (bottom row). The long-term mean net TOA radiation is added back to the anomalies in panel (a) to show net energy imbalance. All variables are defined positive downwards and smoothed by a 12-month moving average for visualization purposes. The values in Figure 1b are equivalent to minus outgoing longwave radiation (−OLR), and the values in Figure 1c are absorbed solar radiation (ASR).

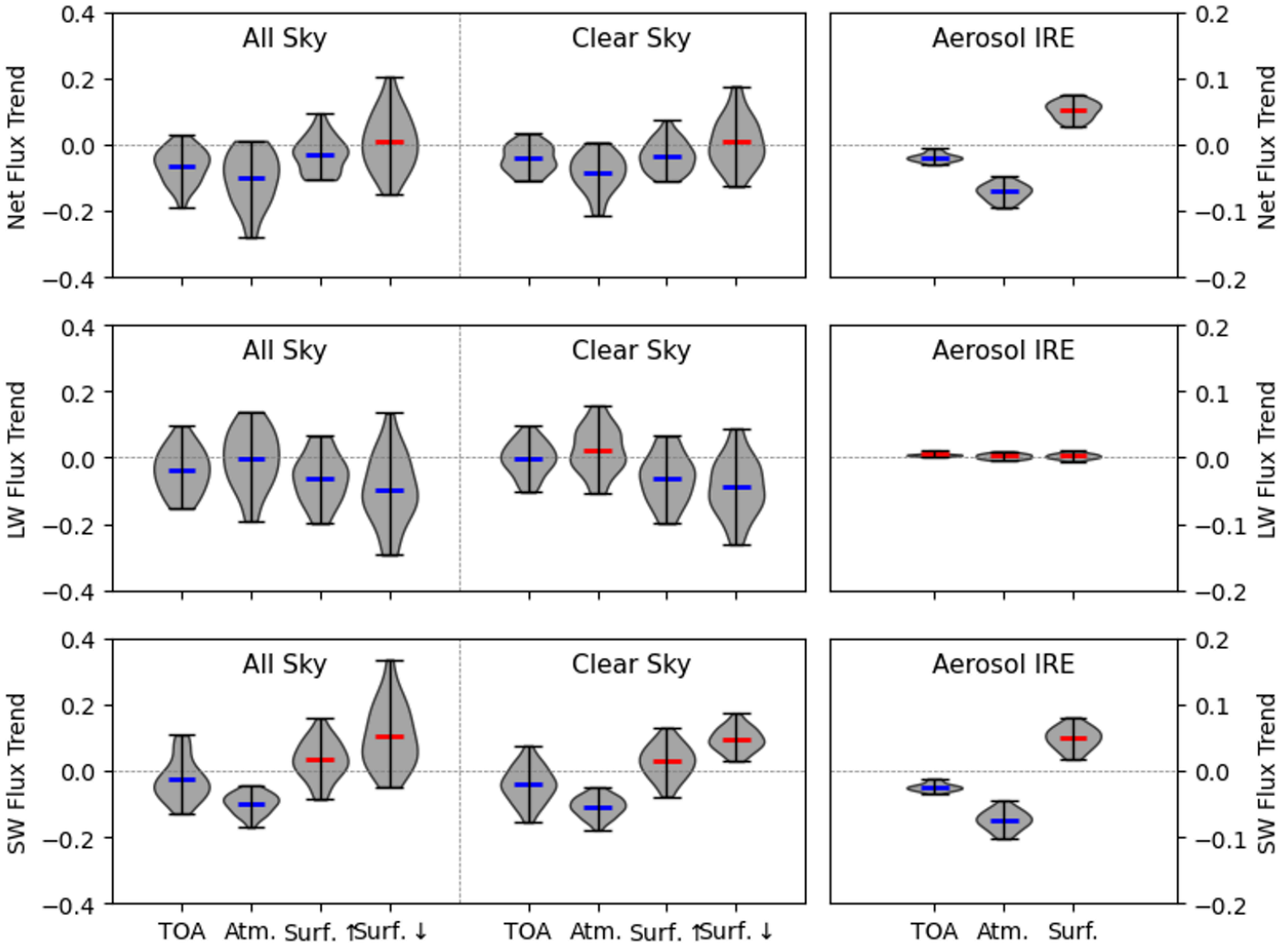


Figure 2

Differences in linear trends (2001~2021) of radiative fluxes from CMIP6 to CMIP7, including TOA radiative fluxes, atmospheric absorption (Atm.), and upward/downward surface radiative fluxes (Surf.). Each violin is computed by subtracting each of the five ensemble members of CMIP7 simulations by each of the five ensemble members of CMIP6 simulations (25 differences in total) and deriving the PDF of the differences. Positive values (red) mean that GFDL AM4 produces more positive trend when using CMIP7 forcing rather than CMIP6 forcing, and vice versa (blue). Longwave flux trend differences (middle row) and shortwave flux trend differences (bottom row) are calculated separately, and the net radiation trend is plotted in the upper row. Atm. is calculated by the difference of the net downward TOA flux and the net downward surface flux. Aerosol instantaneous radiative effect (IRE) is defined as the difference between all-sky flux and clean-sky flux (i.e., without aerosols).

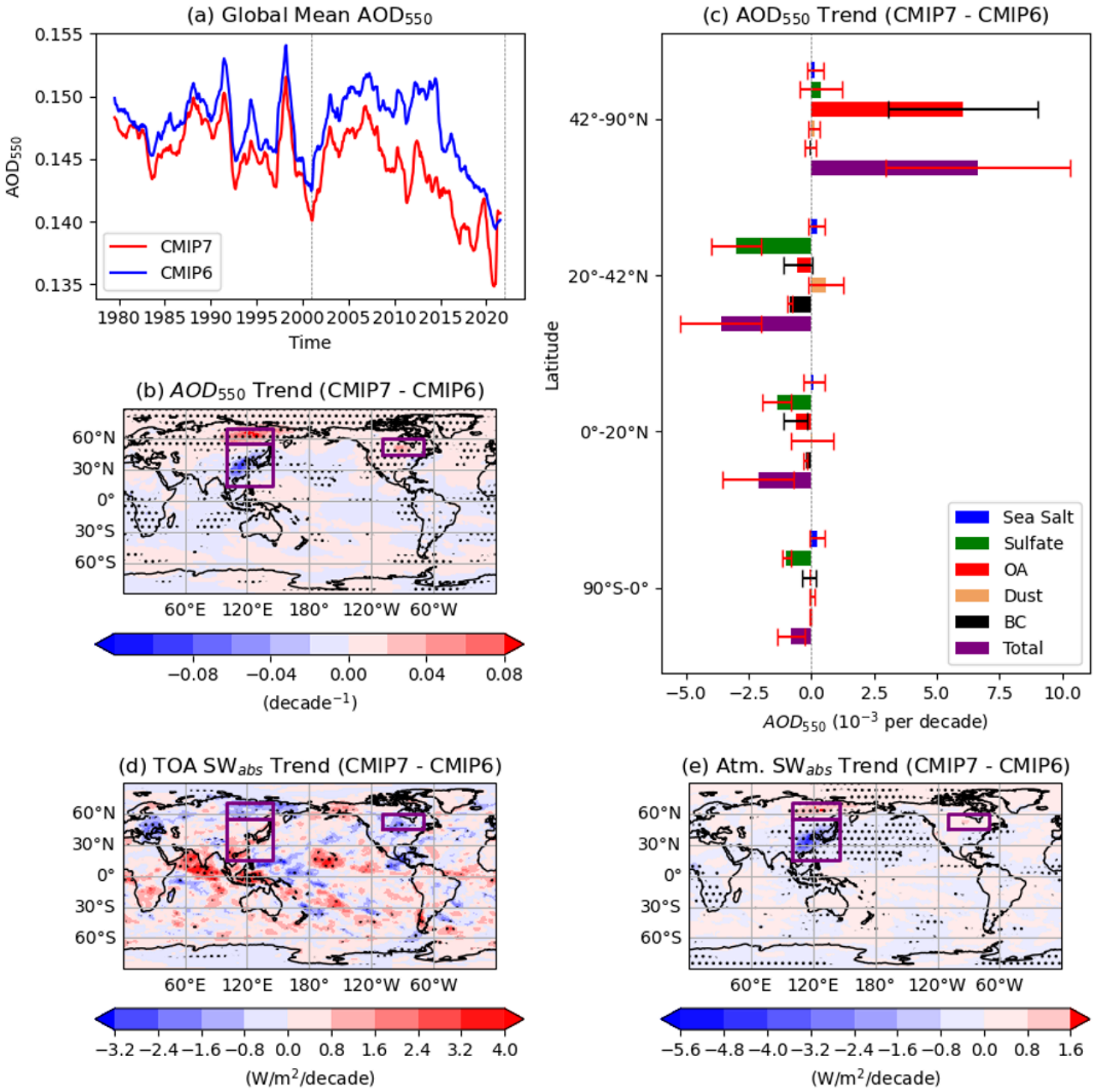


Figure 3

The impact of anthropogenic aerosol forcing updates on Earth's radiation budget. (a) Time series of aerosol optical depth at 550 nm (AOD_{550}) computed by the GFDL AM4 model when using CMIP6 forcing (blue) and CMIP7 forcing (red). Both series have been smoothed by a 12-month moving average for visualization purposes. (b) Spatial pattern of difference of AOD_{550} trend from 2001 to 2021 when CMIP7 forcing is used compared to CMIP6. Dotted region indicates significant trend differences at 95% confidence level. (c) Decomposition of AOD_{550} trend differences into different species of aerosols,

including black carbon (BC), dust, organic aerosols (OA), sulfate, and sea salt, in the Southern Hemisphere and three same-area latitudinal bands in the Northern Hemisphere (i.e., 0°~20°N, 20°N~42°N, and 42°N~90°N). Error bars indicate 95% confidence intervals. (d) Spatial pattern of the trend differences of net TOA SW radiation. (e) Spatial pattern of the trend differences of SW atmospheric absorption. The purple boxes indicate the three regions of interest that will be analyzed later in Section 3.

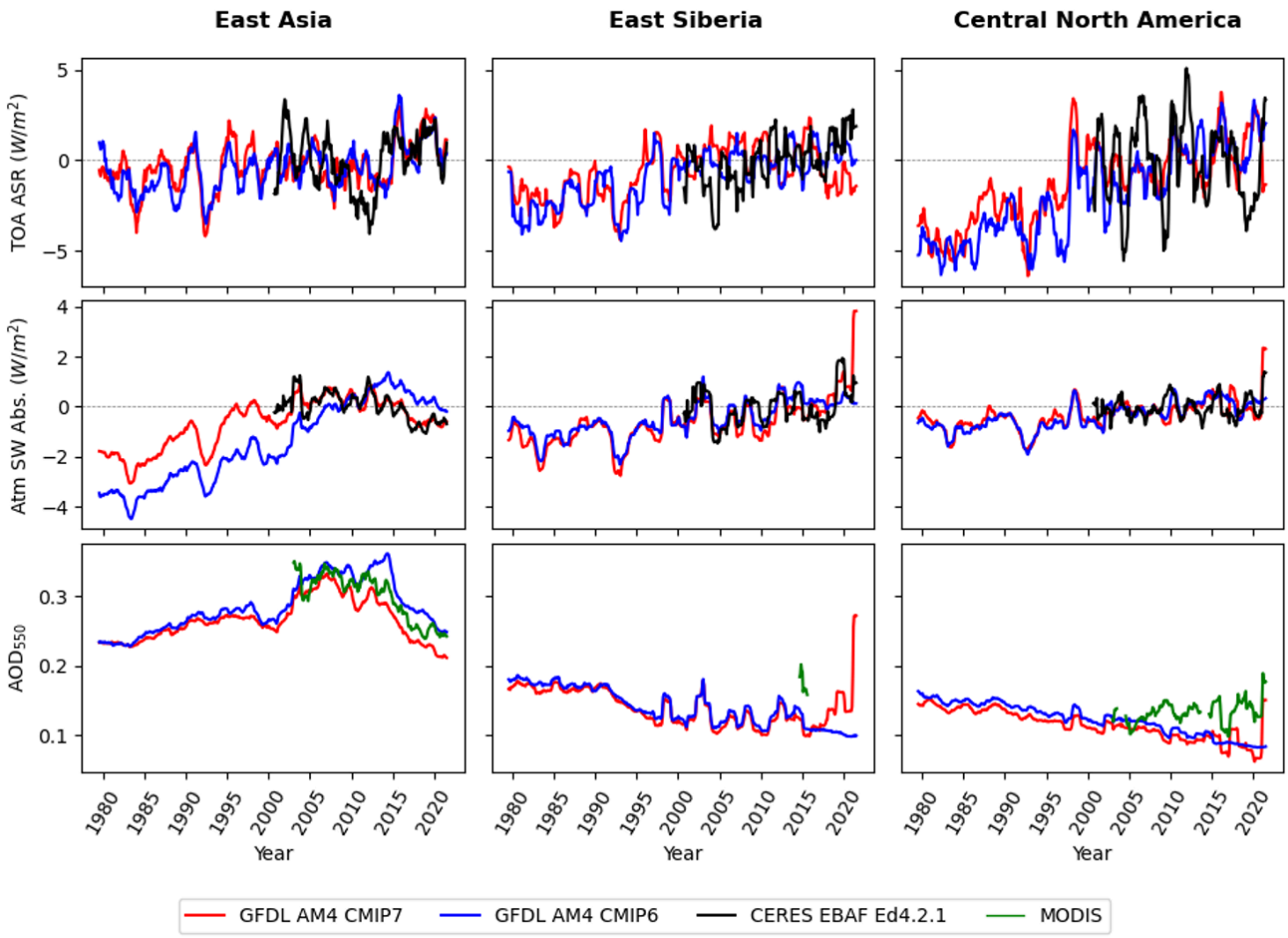


Figure 4

Monthly mean anomalies of absorbed solar radiation at the TOA (top row) and atmospheric SW absorption (middle row), as well as monthly mean AOD at 550 nm (bottom row), over three regions of interest (East Asia, East Siberia, and North America identified in Figure 3) in GFDL AM4 simulations. CERES-observed flux anomalies over the regions are included in the first two rows of panels as black lines. MODIS AOD over the regions is also plotted in the last row. A 12-month moving average is applied to all time series for visualization purposes.

Supplementary Files

This is a list of supplementary files associated with this preprint. Click to download.

- AM4CMIP6vsCMIP7supp.pdf